Journal of Astronomical Telescopes, Instruments, and Systems

AstronomicalTelescopes.SPIEDigitalLibrary.org

Operation of a layer-oriented multiconjugate adaptive optics system in the partial illumination regime

Kalyan Kumar Radhakrishnan Santhakumari
Carmelo Arcidiacono
Thomas Bertram
Florian Briegel
Thomas M. Herbst
Roberto Ragazzoni

SPIE.

Kalyan Kumar Radhakrishnan Santhakumari, Carmelo Arcidiacono, Thomas Bertram, Florian Briegel, Thomas M. Herbst, Roberto Ragazzoni, "Operation of a layer-oriented multiconjugate adaptive optics system in the partial illumination regime," *J. Astron. Telesc. Instrum. Syst.* **5**(4), 049002 (2019), doi: 10.1117/1.JATIS.5.4.049002.

Operation of a layer-oriented multiconjugate adaptive optics system in the partial illumination regime

Kalyan Kumar Radhakrishnan Santhakumari,[a,b,c,*] Carmelo Arcidiacono,[a] Thomas Bertram,[b] Florian Briegel,[b] Thomas M. Herbst,[b] and Roberto Ragazzoni[a]
[a]INAF-Osservatorio Astronomico di Padova, Vicolo dell'Osservatorio, Padova, Italy
[b]Max Planck Institute for Astronomy, Heidelberg, Germany
[c]International Max Planck Research School for Astronomy and Cosmic Physics at the University of Heidelberg, Heidelberg, Germany

Abstract. Multiconjugate adaptive optics (MCAO) promises uniform wide-field atmospheric correction. However, partial illumination of the layers at which the deformable mirrors are conjugated results in incomplete information about the full turbulence field. We report on a working solution to this difficulty for layer-oriented MCAO, including laboratory and on-sky demonstration with the LINC-NIRVANA instrument at the Large Binocular Telescope. This approach has proven to be simple and stable. [DOI: 10.1117/1.JATIS.5.4.049002]

Keywords: adaptive optics; multiconjugate adaptive optics; LINC-NIRVANA; layer-oriented; partial illumination; wavefront reconstruction.

Paper 19015 received Feb. 4, 2019; accepted for publication Sep. 16, 2019; published online Oct. 14, 2019.

1 Introduction

In the late 1980s, Beckers introduced the idea of multiconjugate adaptive optics (MCAO), a technique that could potentially increase the isoplanatic patch substantially.[1,2] The basic principle of MCAO is to use multiple stars measuring the atmospheric volume and correcting the turbulence using $\mathcal{N}$ deformable mirrors (DMs) conjugated to $\mathcal{N}$ layers. Although its feasibility had been earlier tested on-sky,[3,4] the actual implementation of MCAO for nighttime astronomy had to wait until 2007, when the multiconjugate adaptive optics demonstrator (MAD) exhibited various MCAO schemes on the very large telescope.[5,6] Despite a proposed upgrade[7] and plans for future implementations,[8–11] the only currently working nighttime MCAO systems in the world are GeMS at the Gemini South telescope[12,13] and LINC-NIRVANA (LN) at the Large Binocular Telescope (LBT).[14–17]

MCAO systems promise to provide a uniform point spread function (PSF) across a wide field-of-view (FoV), using multiple guide stars, either laser-guide stars (LGSs) or natural-guide stars (NGSs). "Star-oriented"[1,18] and "layer-oriented"[19] are two approaches for implementing MCAO. Star-oriented MCAO uses information from individual wavefront sensors (WFSs), one per star, to computationally estimate the wavefront corresponding to the conjugated layer via tomographic reconstruction of the full turbulence volume. The signals are then sent to the respective DMs to correct the aberrations. In contrast to star-oriented MCAO, layer-oriented MCAO uses one WFS per controlled DM. In other words, light from multiple stars are used by a WFS, which senses the wavefront for a particular conjugation altitude and then drives the corresponding DM.

For both the star- and layer-oriented approaches, NGSs cannot, in general, provide full information of the aberrations in the high-altitude layer since the diverging light paths give incomplete coverage. This can, strictly speaking, also be true for a LGS-based system. However, the arrangement of the LGSs is usually tuned to minimize such effects, and for this reason, we are not going to discuss this case any further. The partial illumination issue can be particularly severe when the wavefront sensing turbulence layer is significantly different from that of the compensated scientific one, especially when combined with a correcting layer at a particularly higher altitude.

In the MAD implementation, the star-oriented approach needed a separate interaction matrix calibration for each asterism. The layer-oriented approach required only one such calibration.[20] Although layer-oriented MCAO has the advantage of computational simplicity compared with star-oriented MCAO, solving the partial illumination issue is a prerequisite for taking advantage of this. Note that for the star-oriented scenario, the partial illumination is addressed by the tomographic reconstruction.

In this paper, we describe a solution to the layer-oriented MCAO partial illumination issue in the context of the LN instrument. Section 2 describes the LN MCAO system and why solving the partial illumination issue is essential. Section 3 explains our solution. Results from laboratory and on-sky tests, along with discussion, appear in Sec. 4. Section 5 concludes with summary and future prospects.

2 Partial Illumination Issue in the Context of the LINC-NIRVANA MCAO System

LN is a high-resolution near-infrared imager mounted at the rear, bent-Gregorian foci of the LBT.[17] LN is equipped with an advanced and unique layer-oriented MCAO module.[21] Wavefront sensing is performed using multiple pyramids, which acquire multiple NGSs from two different FoVs.[22–24] In addition, the design follows the layer-oriented scheme, which foresees the optical co-addition of the star footprints at the WFS, minimizing the read noise penalty and allowing fainter stars to be used for the sensing (as long as the total flux corresponds to the limiting magnitude for correction). We define footprint as the projection of the telescope pupil through which the starlight passes at a given altitude. This approach is expected to increase

*Address all correspondence to Kalyan Kumar Radhakrishnan Santhakumari, E-mail: kalyan.radhakrishnan@inaf.it

the sky coverage in the typical case of being read noise limited.[25] LN can provide uniform 2′ FoV correction for both "eyes" of the LBT, allowing us a larger field from which to choose fringe-tracking reference stars for eventual goal performing Fizeau interferometric imaging.

On each telescope, the atmospheric aberrations are sensed by two WFSs, one conjugated to the ground and the other to a higher altitude, in order to sample the three-dimensional turbulence above the observatory.[26,27] The ground-layer wavefront sensors (GWSs) are conjugated to ∼100 m above the telescope and drive the adaptive secondary mirrors (ASMs, 672 actuators each), using up to 12 natural stars from an annular 2' to 6' diameter FoV centered on the science field. The high-layer wavefront sensors (HWSs) are conjugated to a high altitude, ∼7100 m above the telescope pupil along the optical axis, and drive the two commercial Xinetics DMs (349 actuators each, hereafter high-altitude DMs)[28] mounted on the LN bench. The HWSs can use up to eight stars in the inner 2' diameter FoV to measure the turbulence. LN MCAO correction is purely sequential and the two loops are independent in terms of control. This means that the HWSs receive the ground-layer corrected wavefront, making the loop control simpler, since we may use two separate reconstruction matrices. LN MCAO multiple-FoV approach, where the wavefront sensing is performed using stars lying in contiguous but not overlapping regions, is depicted in Fig. 1.

The reference star light focused at the tip of a four-sided pyramid is split into four beams, forming, through a common optics, four pupil images on the WFS CCD. The pixels may be binned on-chip, depending on the flux of the stars. Binning this way reduces the equivalent readout noise on the individual subapertures. This improvement, coupled with the well-known sensitivity gain,[29,30] is a direct benefit of pyramid wavefront sensing. Comparing the local fluxes in the same subaperture of the four pupil images gives the local tilt.[22] Note that for the ground layer, the nominal star footprints overlap perfectly. Optical co-addition increases the signal-to-noise ratio (SNR) for each subaperture uniformly for the ground layer (the purple shaded region in Fig. 1).

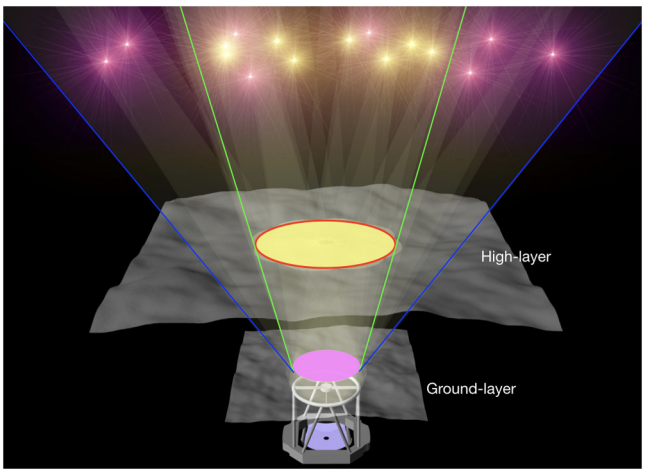

Fig. 1 LN MCAO multiple-FoV approach: The ground layer is sensed using the purple NGSs from the 2' to 6' annular FoV and drives the facility ASM of the LBT. The high layer, conjugated to ∼7100 m away from the telescope pupil along the optical axis, is sensed by the yellow NGSs in the inner 2' diameter FoV. A commercial Xinetics DM on the LN bench corrects the aberrations sensed by the HWS. Note that the yellow shaded region within the red circle denotes the metapupil, and the angle subtended by the green lines and blue lines represent the 2' and 6' FoV, respectively.

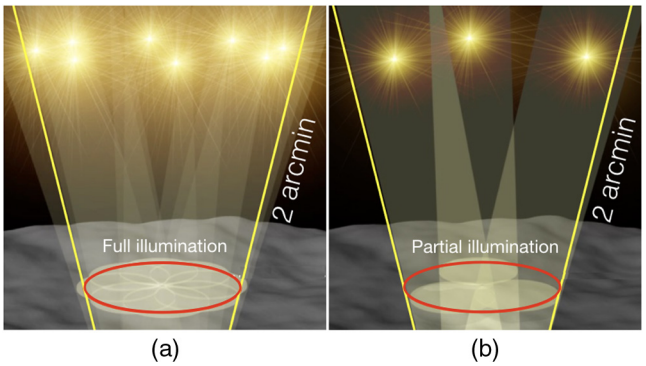

Fig. 2 (a) Full illumination of the metapupil using eight stars. (b) Partial illumination scenario when only three stars are available. Note that, depending on the asterism, the footprints illuminate different parts of the metapupil.

At higher layers, the footprints of the stars are spatially decorrelated, and their positions depend on the star coordinates. In our case, by design, the high-altitude DM covers the footprints from any source within the 2' FoV. This area is called the metapupil. It is the projection of the FoV at the conjugated altitude depicted by the yellow shaded region within the red circle in Fig. 1. For LN, the diameter of the metapupil is about 1.5 times that of a single pupil.

Depending on the asterism, only a part of the metapupil may be illuminated (for example, see Figs. 2 and 3). In this instance, the slopes in the illuminated region can be directly measured, whereas there is no information about the atmospheric aberrations from the nonilluminated part. Since the DM-controlled modes are originally defined over the whole aperture, the stability of the loop, quality of the correction, and uniformity of the PSF in the entire FoV may be affected by this partial illumination situation.[31–34] A solution that can reconstruct the wavefront within the entire metapupil, having information only from

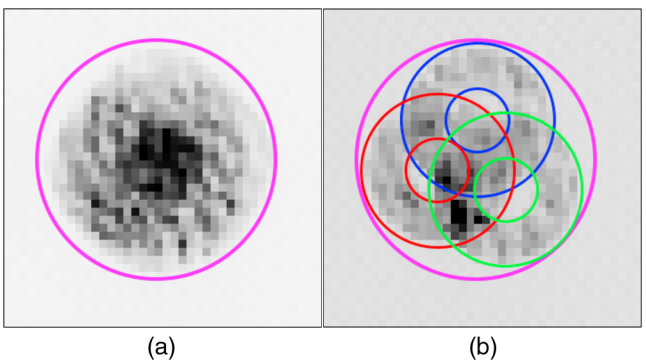

Fig. 3 Images from the HWS CCD, using fibers from the calibration unit as light sources (or stars). (a) Full illumination of the metapupil (magenta circle) using eight stars. (b) An example of the partially illuminated metapupil using three stars. Clearly, the partially illuminated subapertures are a subset of the fully illuminated ones. Note that a star footprint is an annulus rather than a disk. This is because there is a physical mask in the optical path to reduce the sky and background light noise coming from other sources in the FoV that are not acquired for wavefront sensing. This mask blocks 25% of the pupil for the high-layer sensor. There is no additional masking for the ground layer or science channels.

the partially illuminated region, and without wasting precious nighttime for calibration, is the essence of this article.

For optimal correction performance, we need full and homogeneous coverage of the high layer metapupil by the footprint of the NGSs. We aim to fill the 2' diameter FoV with well-distributed, bright ($R_{\mathrm{mag}} \lesssim 15$) stars. Using the expected star density averaged over the sky for the R-band data from the GAIA DR2 catalogue[35–38] and randomly picking fields at $30° \pm 1°$ Galactic latitude, we get 99%, 93%, 82%, and 67% probability to find at least 1, 2, 3, and 4 stars, respectively, for the GWS FoV. Similarly, for the HWS FoV, it is 41%, 11%, 2%, and <0.1% probability to find at least 1, 2, 3, and 4 stars, respectively. For this estimation,[25] we have used stars with $R_{\mathrm{mag}} \lesssim 15$ and an avoidance zone of 10" radius around each pyramid. Typically, we operate with three stars or fewer, pushing us to adopt a reliable and high-performance solution to the partial illumination issue.

Furthermore, the LBT is an alt-azimuth telescope. As a result, LN has to deal with changing parallactic angles as the sky is rotating. Each WFS is equipped with a derotation mechanism. There is a K-mirror derotator,[39–41] after the high-altitude DM in the optical path and before the HWS (see Fig. 4). Note that the derotation continuously changes the mapping between the WFS subapertures and the DM actuator pattern. This necessitates uploading of the appropriate reconstruction matrix on-the-fly, for every $\theta°$ of sky rotation. For our system, $\theta° = 1$ deg of sky rotation.[43,44] This arrangement has the advantage that the position of the stars does not change in the focal plane of the WFS. Therefore, the illumination region also remains unchanged.

In typical AO systems, modal control of the DM is performed. The WFS slope vector multiplies with the reconstruction matrix to obtain the modal coefficients. In such AO systems, where all the subapertures are illuminated (full illumination), the WFS uses one reconstruction matrix for any asterism of stars to deduce the commands to drive the DM for a given field rotation angle. However, for a partially illuminated scenario, the use of the reconstruction matrix derived for the fully illuminated metapupil will result in improper correction. Note that, in our current operating mode, the modal basis is defined over the entire metapupil. For the high spatial frequency modes, the modal information lies in rather closely spaced subapertures. If the illuminated regions do not cover these subapertures, using the reconstructor corresponding to the fully illuminated metapupil will result in incorrect modal coefficients, generating spurious commands to the DM. This worsens the science image as well. Although perhaps obvious, we have tested this situation in the lab. Indeed, the performance was reduced by triggering the interactuator stroke limit (the maximum "push-pull" value admissible between two neighboring actuators) or driving the actuators out of range.

We designed an algorithm to generate the reconstruction matrix corresponding to the current illumination pattern in real time from previously calibrated (daytime) data for the fully illuminated metapupil, according to the prevailing K-mirror angle. Section 3.2 below provides further details.

3 Our Solution

3.1 *Experimental Setup*

The experimental setup used for developing and testing our solution to the partial illumination issue is the fully integrated and aligned LN bench (see the right image in Fig. 4). Figure 5 shows the LN calibration unit. It consists of a folding mirror (CU-mirror), an absolute reference fiber (ARF), a reference fiber plate (RFP), and an integrating sphere (IS). The CU-mirror is

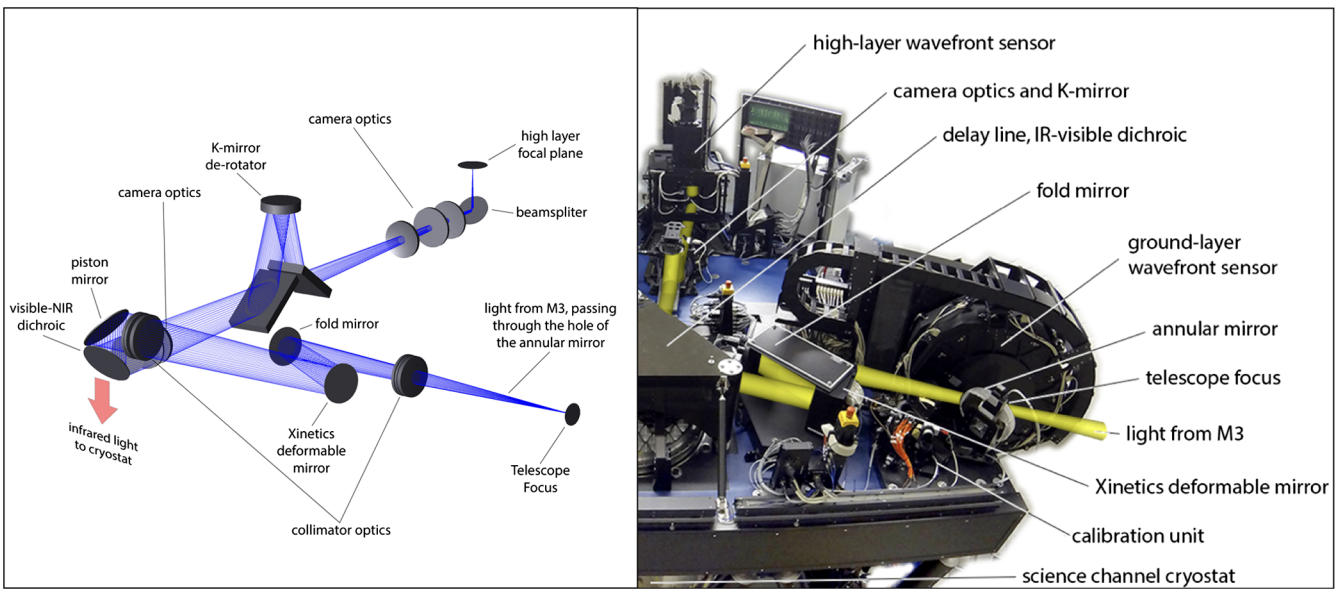

Fig. 4 The LN bench and optical path: tertiary mirror (M3) of the LBT directs the light to the LN bench. At the first encounter by the annular mirror, the 2' to 6' diameter annular FoV is directed toward the GWS, whereas the inner 2' continues through the collimator, folding mirror, the Xinetics deformable mirror, piston mirror, to the IR-visible dichroic. The infrared light enters the cryostat below the optical bench while the visible part continues to the HWS via a K-mirror (for field derotation) and other optical elements. The optical path is the same for the other side. See Herbst et.al.[42] for more details. While the right image shows the actual bench populated with components, the left image explicitly shows the various components on the bench.

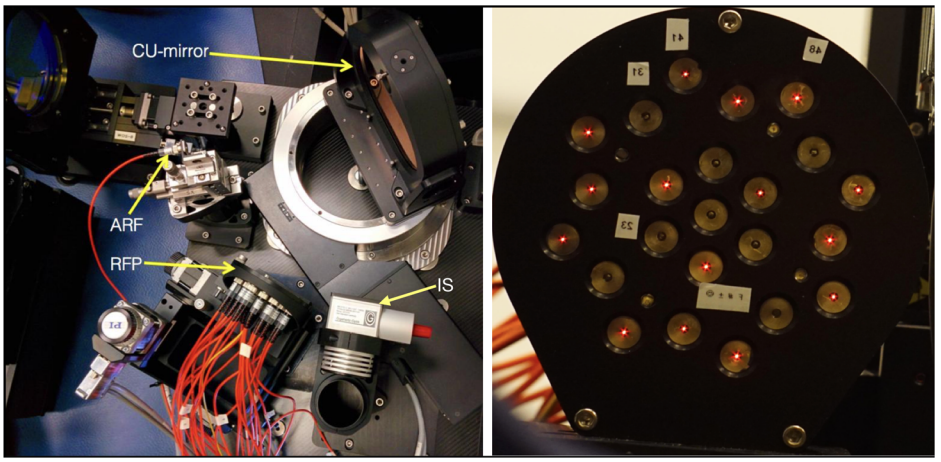

Fig. 5 (a) Calibration unit on the LN bench, consisting of a folding mirror, a reference fiber, a fiber plate, and an IS. (b) Front view of the fiber plate. Some of the fibers are (red) illuminated.

mounted on a precision rotation stage that allows us to direct the calibration unit light to the HWS. The ARF defines the on-axis telescope beam. The RFP is mounted on a tip-tilt stage, which can also move along the three axes. The RFP has 23 fibers mounted to it, defining a set of "stars" in the 2' FoV. The central star is a monomode near-infrared fiber, whereas the reminder are multimode 200-μm (0".33 on the sky) fibers fed by visible-wavelength LEDs. The intensities of the fibers can be individually and remotely controlled. We can thus generate defined stellar asterisms and vary their brightness. Note that the RFP is slightly concave, mimicking the curved focal plane of the LBT. The IS is used for flat-fielding.

The fully illuminated metapupil is generated by illuminating the eight outermost fibers in the RFP. Each of the fibers is calibrated for brightness in real, on-sky magnitudes. For calibration purposes, the fiber intensity of each of the eight stars is set to $R_{\mathrm{mag}} \sim 6$. This ensures good SNR at the HWS CCD while avoiding saturation. The HWS has eight probes (see Fig. 6) that can move in the 2' FoV to acquire and center on the stars. Using the fiber plate and the HWS probes, it is possible to calibrate the HWS, create partial illumination test cases, evaluate our algorithm, and optimize the high-layer loop.

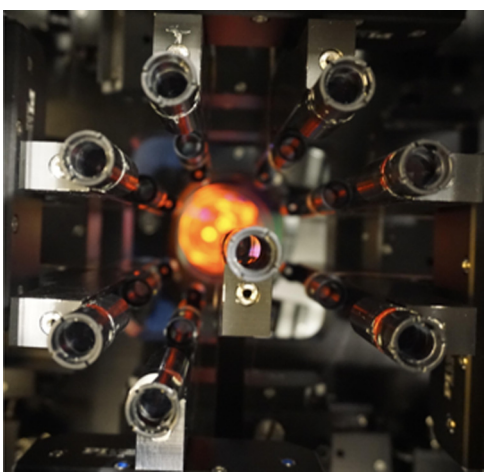

Fig. 6 The eight probes in the HWS can move over the focal plane to acquire the stars in the 2' FoV. The minimum separation to avoid collisions corresponds to 20".

3.2 *Strategy*

In order to close the AO loop, we need to have the correct combinations of the following four matrices:

(1) The modes to command matrix ($\mathbb{M}2\mathbb{C}$) is the response of the DM to the orthonormal modal base. It has dimensions of (number of actuators × number of modes). There will be specific actuator values defining each mode across the DM. When multiplied with the modal coefficient vector, $\mathbb{M}2\mathbb{C}$ produces the commands to be sent to the DM. In our case, the modal basis is the Karhunen–Loéve[45] (KL) projected on the DM space, recognizing the Kolmogorov statistics and the actuator positions on the DM.

(2) The interaction matrix ($\mathbb{IM}$) is the response of the WFS to the DM and has dimensions of [(2× number of subapertures) × number of modes]. There is a relationship between the WFS subapertures and the DM actuators, depending on the binning of the WFS CCD. Each subaperture corresponds to two adjacent rows of the $\mathbb{IM}$, one for each of the orthogonal axes of the slope vectors. The information of how much the DM has to change its shape to produce a specific slope measurement is encoded in the $\mathbb{IM}$.

(3) The reconstruction matrix ($\mathbb{RM}$) or the reconstructor is the pseudoinverse of the $\mathbb{IM}$ and therefore has dimensions of [number of modes × (2× number of subapertures)]. The modal coefficient vector is the product of the measured slope vector and the reconstructor.

(4) The illumination mask ($\mathbb{M}$) is the image that defines the illuminated subapertures. Without on-chip binning (i.e., binning = 1), the number of subapertures for a fully illuminated metapupil is about 616. The length of the measured slopes vector is two times

the number of illuminated subapertures. In most AO systems, this is fixed. However, in our case, the vector length varies.

It is essential to incorporate or "register" the correct combination of the $\mathbb{M}2\mathbb{C}$, $\mathbb{IM}$, or $\mathbb{RM}$, and $\mathbb{M}$ in the loop. In our case, the $\mathbb{M}2\mathbb{C}$ is always the same, whereas $\mathbb{IM}/\mathbb{RM}$ and $\mathbb{M}$ vary according to the observed target.

In order to determine if a subaperture is well illuminated or not, we need to know the SNR. Although the major components of flexure are compensated by the CCD positioning algorithm,[46] there are factors that favor the $\mathbb{M}$ created out of SNR thresholding over using geometrical arguments. One of the main reasons is the following. The amount of light actually reaching the detector will vary according to the seeing since the pyramid FoV is limited (to 1".1 in diameter). If the stellar magnitudes and the colors mentioned in the catalog are different from the actual values, the seeing variation may actually create differential illumination at the detector. We, therefore, chose an SNR threshold criterion that is easy and quick to determine if a subaperture is illuminated or not.

As the first step for identifying the illuminated pixels, we acquire sky background frames (these are in any case needed for wavefront sensing later). All the probes that have acquired the high-layer reference stars are temporarily moved a short distance to their so-called shadow-positions, where the starlight is blocked by the probes and does not reach the HWS CCD. At this point, $\mathcal{F}$ sky frames are taken. The GWS is in closed-loop while the high-layer probes are individually centered (averaging well over the turbulence, with a precision close to one-tenth of an arc sec) and later while taking the $\mathcal{F}$ sky frames. A pixel-by-pixel standard deviation of these $\mathcal{F}$ sky frames forms the noise image. The probes are then sent back to their centered positions and $\mathcal{F}$ illuminated frames are taken. A pixelwise median of these $\mathcal{F}$ frames gives the partial illumination image. The SNR image is then created using the following:

$$\mathrm{SNR}_{\mathrm{img}} = \frac{\widetilde{P_{\mathrm{img}}}}{\sqrt{\widetilde{P_{\mathrm{img}}} + (\widetilde{N_{\mathrm{img}}})^2}}, \tag{1}$$

where $\widetilde{P_{\mathrm{img}}}$ is the four-quadrant sum of the partial illumination image P_{img}, and $(N_{\mathrm{img}})^2$ is the square of the noise image. $\widetilde{P_{\mathrm{img}}}$ is given by

$$\widetilde{P_{\mathrm{img}}} = \sum_{\mathrm{quadrant}=1}^{4} (P_{\mathrm{img}})_{\mathrm{quadrant}}. \tag{2}$$

The pixels in the $\mathrm{SNR}_{\mathrm{img}}$ with values higher than a given threshold will be masked to 1 and others to 0, creating $\mathbb{M}$. Typically, the value of $\mathcal{F}$ we use is 1000.

Depending on the HWS CCD binning and the seeing, the right SNR criterion has to be used. We have a look-up table for this, which is created empirically in open-loop looking to the behavior in closed-loop. During the observation, we patrol the illumination to take care of the mispositioning of the probe due to flexures. Note that any partially illuminated mask created by the SNR threshold criterion will be a subset of the fully illuminated mask. Figure 3 illustrates this.

Section 2 explains why we cannot use the same $\mathbb{RM}$ as for full illumination. In our solution, depending on the illuminated region, a new $\mathbb{IM}$ is extracted from the fully illuminated $\mathbb{IM}$ for the current K-mirror angle. We name the fully illuminated $\mathbb{IM}$ the "mother interaction matrix" (mother-$\mathbb{IM}$) and the reduced, partially illuminated one the "daughter interaction matrix" (daughter-$\mathbb{IM}$). The following subsections present the details of the calibration of the mother-$\mathbb{IM}$ and the extraction of the daughter-$\mathbb{IM}$.

3.2.1 *Calibrating the mother interaction matrix*

Our partial illumination algorithm depends fundamentally on a well-calibrated, fully illuminated, well-conditioned mother-$\mathbb{IM}$ for the given $\mathbb{M}2\mathbb{C}$. The condition number describes the sensitivity of a function to changes or errors in the measurement data. In other words, the condition number is a proportionality factor in the error. The higher the condition number of a matrix, the more singular or rank deficient is the matrix. For a well-conditioned matrix, the noise propagates smoothly over the Eigen modes, and the condition number will be small.

For the calibration, we use SNR threshold of 20 to identify the illuminated subapertures. This SNR threshold is for a set of $R_{\mathrm{mag}} \sim 6$ "stars" illuminating the full metapupil. After acquiring and centering the eight HWS star probes on the eight fibers in the outermost ring of the RFP, we measure the actual illumination on the metapupil.

Having set the corresponding $\mathbb{M}$, we then run the $\mathbb{IM}$ calibration script. We apply the push–pull history of the modes defined by the $\mathbb{M}2\mathbb{C}$ to the high-altitude DM and measure the corresponding slopes.[44] Analyzing the slopes, we extract the $\mathbb{IM}$. The calibration procedure is laid out as a flowchart in Fig. 7. First, we calibrate for two modes (tip and tilt). Once we have the corresponding $\mathbb{IM}$, we close the loop for the two modes and download the actuator commands (dmCommands). The average of the dmCommands, when added to the "DM-flat" (the shape of the DM closest to a perfect plane mirror), will give us the shape of the DM corresponding to the "pyramid-flat." Note that the DM-flat measured during the alignment using an interferometer is used as the starting point. However, the pyramid-flat provides the HWS with the right shape to remove static aberrations in the optical path. Running the calibration on the pyramid-flat is superior to doing so on the DM-flat since this increases the pyramid sensitivity, avoids WFS saturation, and makes the pyramid working as close as possible to the diffraction-limited regime.

We then proceed to calibrate higher and higher numbers of modes, following the same procedure, each time refining the pyramid-flat. At the same time, the number of iterations (shown as yellow dotted line in Fig. 7) is increased so that the SNR is sufficient. The number of iterations is large enough to compensate the Poisson noise and fast turbulence/vibrations at the LBT but not too large to avoid the inclusion of slow drift of any motors within LN. Finally, we get a well-conditioned mother-$\mathbb{IM}$. For example, we typically have a condition number of 25 for 200 modes for the mother interaction matrices.

The K-mirror can compensate for up to 180 deg of sky rotation. As mentioned earlier, the derotation necessitates uploading the reconstructor for every $\theta°$ of sky rotation. This, in turn, means that there should be a mother-$\mathbb{IM}$ for every $\theta°$. Each of these mother-$\mathbb{IM}$s should have similar quality and SNR. Actually, the calibration is performed for only six different angles. These six angles are chosen knowing the actuator spacing so that the smoothing effect inaccuracy is minimal.[43] Each of the calibrated measurements are then numerically rotated to

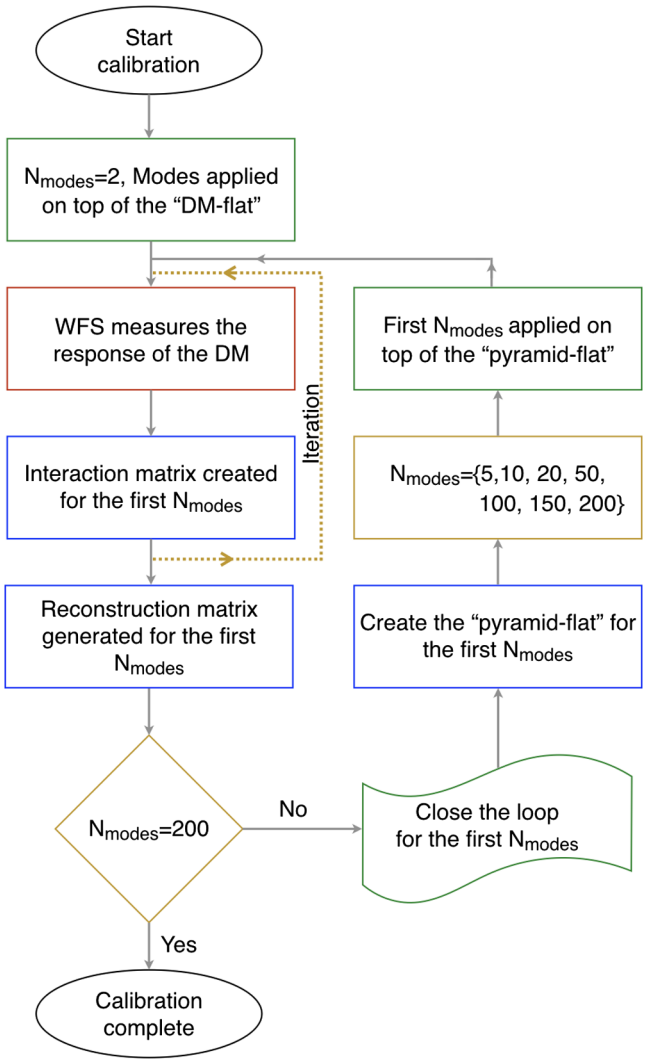

Fig. 7 Flowchart explaining the calibration procedure of the mother-$\mathbb{IM}$ for 200 modes. A Python script communicates with the instrument and performs the calibration in an almost fully automatic way.

each integral degree. The average of the six numerically rotated measurements forms the final mother-$\mathbb{IM}$ for each angle.

3.2.2 *Extracting the daughter interaction matrix*

As described in Sec. 3.2 above, there will be a unique $\mathbb{M}$ for each asterism. It is essential to have the correct $\mathbb{IM}$ matching the $\mathbb{M}$ to close the loop. Calibrating a new $\mathbb{IM}$ for each asterism would consume a lot of observing time. To avoid this, we came up with the following algorithm.

For each angle, the mother-$\mathbb{IM}$ contains the slope response for every subaperture and calibrated mode. The subapertures illuminated in the partially illuminated case are of course illuminated in the fully illuminated case as well. Removing those rows in the mother-$\mathbb{IM}$ corresponding to the nonilluminated subapertures generates the daughter-$\mathbb{IM}$. Figure 8 illustrates this schematically. Inverting the daughter-$\mathbb{IM}$ produces the $\mathbb{RM}$ for that particular partial illumination case. This calculation is very fast and is done during observing, whenever there is $\theta°$ change in sky rotation or a change in $\mathbb{M}$. This $\mathbb{RM}$ is registered to close the loop for the respective $\mathbb{M}$.

Recall that the KL modal base is defined over the entire metapupil. This means that, ideally, we should get the modal coefficients from the slopes spread across the entire metapupil. However, we have only a subset of the slopes due to partial illumination. From these measured slopes, we should retrieve the modal coefficients. The extracted daughter-$\mathbb{IM}$ has the corresponding slope values of the present illuminated mask for each mode. The respective reconstructor, when multiplied to the measured slope vector, will produce the modal coefficients from the limited information for the whole metapupil.

We emphasize that the Kolmogorov statistics are implicitly incorporated in the KL basis command matrix ($\mathbb{M}2\mathbb{C}$). The extrapolation produced by our algorithm, therefore, takes advantage of the spatial correlations based on the Kolmogorov statistics. However, as mentioned by Véran in his paper,[47] there is a possibility of saturation (of the actuator range) for the non-illuminated actuators, and this issue could be mitigated using a "leaky integrator." This is not yet implemented in our system. We are looking into the possibility of implementing a leaky integrator within our current real-time computer framework.

The effect of lack of information cannot be ignored. Generating a $\mathbb{RM}$ from the daughter-$\mathbb{IM}$ will have a higher condition number. If the condition number is very large of the order of 10^3 or higher (from our experience), then the matrix is said to be ill-conditioned. For a high condition number matrix, small measurement errors will translate to large actuator errors, which can cause divergence or instability. The higher the condition number, the lower the number of modes that can be corrected in a stable loop. In particular, the high spatial frequency modes that require information from closely spaced subapertures, which are not illuminated, may not be corrected. Depending on the number of illuminated pixels, the user may decide to use only a subset of modes for the extraction, starting from the mother-$\mathbb{IM}$. For example, the user can decide to correct for only the first 50 modes instead of all 200 modes. The number of modes used for correction places an upper limit to the Strehl ratios (SRs) that can be achieved. In addition, the AO system will have little control over the Strehl in those regions where there is no illumination.

Our commissioning experience so far shows evidence that this algorithm works fine, both in the laboratory and on-sky.

4 Laboratory and On-Sky Tests

4.1 *Laboratory Tests*

We performed tests in the laboratory to verify and optimize the partial illumination algorithm. All these experiments were performed in the bright-end regime. The goals of these tests were (1) to determine the effect of the selection of subapertures and the impact of reasonable variation in the SNR threshold on the correction, (2) to determine differences in getting the reconstructor from the daughter-$\mathbb{IM}$ with and without truncation in the singular value decomposition (SVD), and (3) to quantify the quality of correction as a function of the illuminated subapertures.

In these following tests, we introduced a known disturbance [i.e., dynamic wavefront error (WFE)] on the high-altitude DM, imitating the turbulence in the high layer. The actuators apply this simulated turbulence following the Kolmogorov power spectrum evolving with a wind speed of 10 m/s. The simulated turbulence assumed the Taylor's frozen flow hypothesis. Note that when observing, the HWS receives the ground-layer

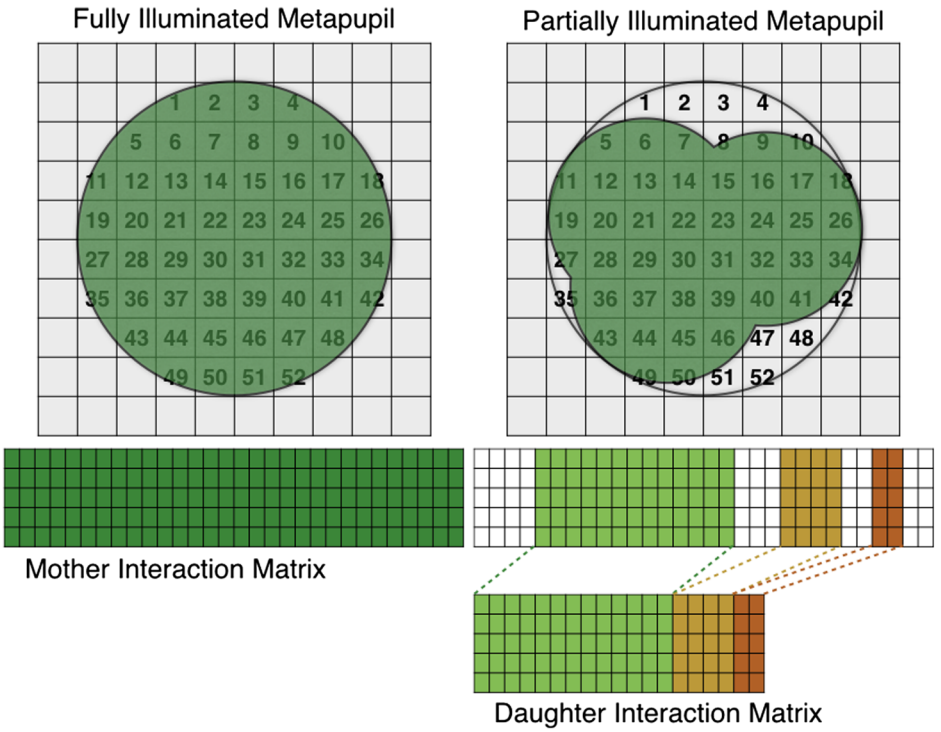

Fig. 8 A schematic diagram explaining the extraction of the daughter-$\mathbb{IM}$ from the mother-$\mathbb{IM}$. On the left, the fully illuminated metapupil and the corresponding $\mathbb{IM}$ can be seen. On the right, the partially illuminated metapupil appears along with the daughter-$\mathbb{IM}$ extracted out of the mother-$\mathbb{IM}$.

corrected wavefront. We selected a disturbance with a root mean square (RMS) WFE of ∼550 nm after the ground-layer correction. Later, we obtained similar residual RMS WFE values after the ground-layer correction on good seeing conditions (0".7 in V-band).

4.1.1 *Impact of reasonable variation in the SNR threshold on the correction*

The SNR threshold will define if a subaperture within the metapupil is illuminated or not. We wanted to verify how sensitive the quality of the correction is to the SNR threshold. In particular, the impact of losing the outermost subapertures is due to the SNR threshold value for a bright asterism. This verification is necessary since the quality of the correction can otherwise vary a lot, and the stability of the loop may be affected.

For this test, we considered two cases: (1) eight stars asterism, corresponding to full illumination and (2) three stars asterism, corresponding to a partial illumination scenario. For both cases, all of the stars were of $R_{\mathrm{mag}} \sim 6$ equivalent brightness. A dynamic WFE of 536 nm was applied to the high-altitude DM to check the correction performance.

Each calibrated mode has its own gain, and together, these values form the gain vector. Typically, we split the modes into three groups—tip and tilt (modes 1 and 2), modes from 3 to 50, and modes higher than 50. Each of these groups were given an individual constant gain value while closing the loop. For each SNR threshold value trial, we optimized the gain vector to produce the best, stable correction.

The quality of correction is quantified by the residual RMS modal coefficients and by the residual RMS WFE. The RMS modal coefficients can be estimated in two ways: (a) directly from the residual wavefront slopes (by multiplying with the $\mathbb{RM}$) and (2) from the dmCommands computed over the full metapupil (by multiplying with the $\mathbb{M}2\mathbb{C}$). We used the second one as it provides the residual over the entire metapupil and not just the illuminated part. The RMS WFE is evaluated from the modal coefficients, as the quadrature sum of the RMS modal coefficients.

Different SNR threshold values result in slightly different masks, differing, of course, in the number of subapertures illuminated. The reasonable SNR threshold range was defined such that the geometrical projection of the stars on the HWS CCD and that on the sky are very close, and only the subapertures at the edges of the pupils were affected. In the full illumination case, the SNR threshold range was 10 to 25, for which the number of selected subapertures ranged from 616 to 588. Similarly, for the partial illumination case, the SNR threshold range was 5 to 20. The corresponding number of subapertures ranged from 528 to 484.

The effect of the different SNR thresholds on the correction for the two cases appears in Fig. 9, where the RMS value of the modal coefficients is plotted against the modes. The black dashed line is the open-loop with an RMS WFE of 536 nm. The solid lines, in different colors, represent the performance for different reasonable SNR threshold values. For both the full and partial illumination cases, there is a clear improvement, independent of the SNR threshold, reducing the WFE to ∼65 and 125 nm, respectively. This means that for the bright-end regimes, the correction is not sensitive on the actual SNR threshold value used, as long as it is within a reasonable range, for both full and partial illumination scenarios.

4.1.2 *Partial illumination reconstructor with and without truncation in the singular value decomposition*

Section 3.2.2 describes the extraction of the daughter-$\mathbb{IM}$ from the respective mother-$\mathbb{IM}$. The inverse of the daughter-$\mathbb{IM}$ to get

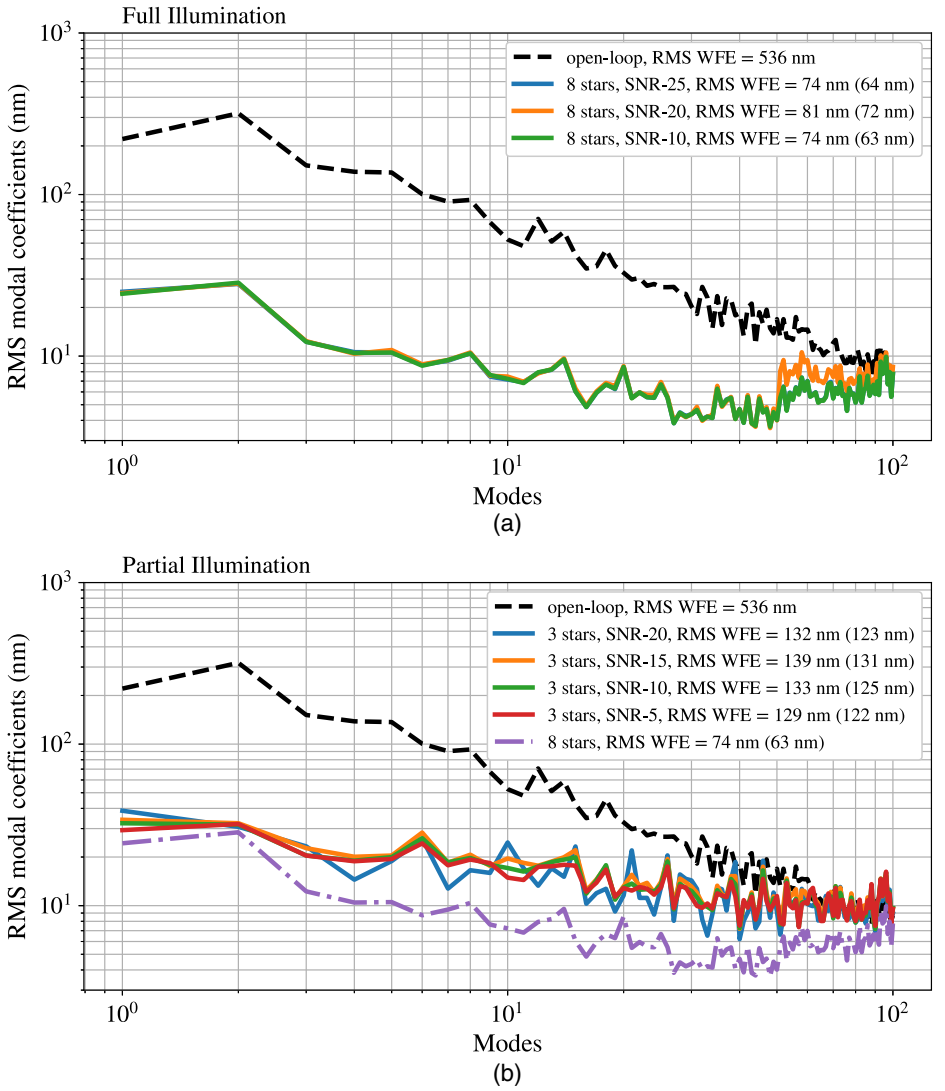

Fig. 9 RMS value of the modal coefficients versus the modes for the case of (a) full illumination using eight stars and (b) for partial illumination using three stars. The dashed line represents the open-loop data, and the solid lines are the closed loop performance. The different colors represent different SNR threshold values for selecting the illuminated subapertures. The RMS WFE are mentioned in the legend. The value in brackets is the RMS WFE excluding the tip and tilt modes.

the corresponding $\mathbb{RM}$ can be done using SVD through the Moore–Penrose method.[48,49] In the process of SVD, many of the eigenvalues, not zero, can become quite small, causing the inversion to diverge in presence of noise. To prevent this, the SVD may be truncated using a defined threshold value. Such a reconstructor is called the "truncated singular-value-decomposed reconstructor" (hereafter, truncated reconstructor).

We tested whether the truncated reconstructors are superior to the nontruncated ones. This was performed by measuring the quality of correction for defined partial illumination cases with reconstructors created with and without truncation but with the same set of gain values for both cases. In order to maintain the noise propagation similar to that of the mother-$\mathbb{IM}$, we opted for the following normalization of the threshold applied for the Eigenvalue truncation:

$$\mathrm{TSVD}_{\mathrm{threshold}} = \left(\frac{\mathrm{S}^{\mathrm{d}}_{\mathrm{max}}}{\mathrm{S}^{\mathrm{m}}_{\mathrm{max}}}\right).\mathrm{S}^{\mathrm{m}}_{\mathrm{min}} \tag{3}$$

where $\mathrm{S}^{\mathrm{d}}_{\mathrm{max}}$, $\mathrm{S}^{\mathrm{m}}_{\mathrm{max}}$, and $\mathrm{S}^{\mathrm{m}}_{\mathrm{min}}$ are the maximum singular value of the daughter-$\mathbb{IM}$, maximum singular value of the mother-$\mathbb{IM}$, and minimum singular value of the mother-$\mathbb{IM}$, respectively.

Two different cases were considered: (1) eight stars asterism and (2) two stars asterism. In each case, the individual stars' were set to $R_{\mathrm{mag}} \sim 7$. A disturbance with average dynamic WFE of 536 nm was applied to the high-altitude DM.

Table 1 lists the number of subapertures illuminated, the condition numbers, the number of modes truncated during the SVD, and the number of modes that could be corrected for a stable closed loop for both truncated (TSVD—ON) and nontruncated (TSVD—OFF) scenarios. Obviously, for the nontruncated cases, none of the modes are truncated. Also, you may note that the number of subapertures is slightly different for the truncated and nontruncated cases with two stars. This is because each of the runs were ran independent, resulting in slightly different $\mathbb{M}$.

The quality of correction is quantified using the RMS value of the modal coefficient values. The modal coefficients were estimated by multiplying the dmCommands by the $\mathbb{M}2\mathbb{C}$,

Table 1 Comparison between truncated and nontruncated reconstructors.

		Eight stars	Two stars
TSVD—OFF	No. of subapertures	616	309
	Condition #	8.93	222.18
	No. of truncated modes in the reconstructor	N/A	N/A
	No. of modes corrected in closed loop	100	2
TSVD—ON	No. of subapertures	616	334
	Condition #	8.93	185.90
	No. of truncated modes in the reconstructor	0	18
	No. of modes corrected in closed loop	100	10

producing the modal coefficients corresponding to the entire metapupil.

Clearly, Fig. 10 shows that using the truncated reconstructors is superior to the nontruncated ones for the two stars asterism, illuminating 310 subapertures. Ten modes were corrected stably with the truncated reconstructor, whereas only the first two modes were stable without truncation. Note that, for this test, we marginally optimized the gain vector. We used a set of predefined gains, the same for both the truncated and nontruncated cases. Using different gains, it is possible to control more modes for the truncated-SVD scenarios, but this approach provides little improvement in the nontruncated case since the optimal gains will be too small.

Here, we have explained only limiting cases (eight stars and two stars). From this result, coupled with our experiences on laboratory and on-sky, we come to the conclusion that the impact of the truncated reconstructors is significant for low-number asterisms. The difference in the quality of correction due to the truncated and nontruncated reconstructor becomes smaller as the $\mathbb{M}$ gets closer to full illumination, which is clear from the eight stars case. However, truncation removes low sensitivity modes, therefore improving the AO-control by reducing the noise propagation. We conclude that using the truncated reconstructors is preferred. The LN software implements this algorithm, always producing a truncated reconstructor with the threshold defined by Eq. (3).

4.1.3 *Closed loop performance as a function of the number of illuminated subapertures*

We tested our partial illumination algorithm with asterisms containing different numbers of stars. Of course, this also means a different number of illuminated subapertures in each case.

As with the previous tests, all the individual stars were set to $R_{\mathrm{mag}} \sim 7$, and the SNR threshold was set to be 20. For each asterism, the $\mathbb{M}$ and the corresponding truncated reconstructor were set to the loop. The RMS value of the modal coefficients was used as the merit function to assess the quality of the correction.

Seven different cases were investigated and optimized, starting from eight stars to two stars. The number of subapertures illuminated varied from 596 to 410 subapertures. For the three-star and two-star scenarios, the reconstructors were created by truncating one and five modes, respectively. You may note that compared to the previous experiment, where the two stars asterism illuminated 310 subapertures, in here 410 subapertures are illuminated. This is because, in this experiment, we have used more separated stars. Also, in comparison to the previous experiment, the gain vector was optimized for individual cases, allowing us to close the maximum number of modes.

Figure 11 displays the RMS value of the modal coefficients as a function of the modes for the different asterisms. Clearly, as the number of subapertures increases, the correction is better.

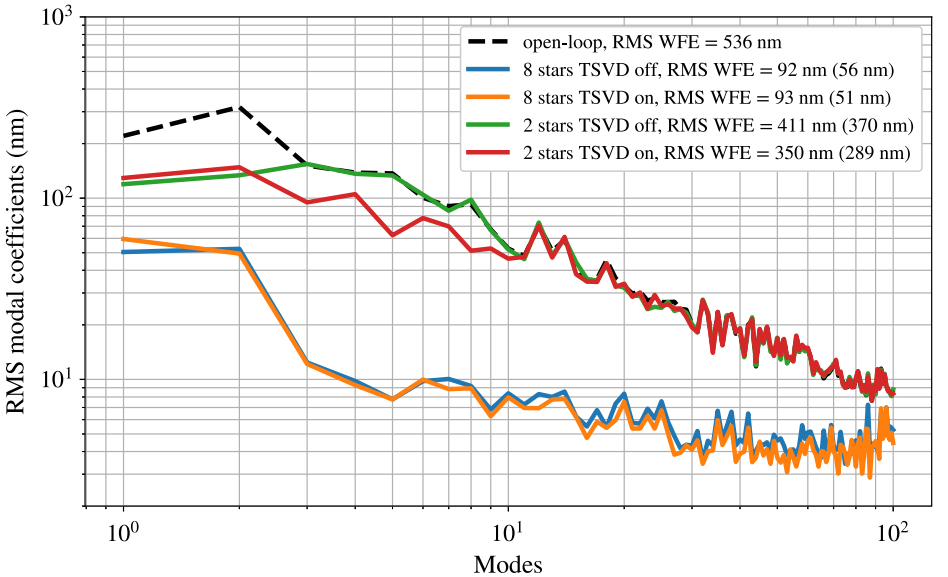

Fig. 10 The RMS value of the modal coefficients versus the modes using truncated and nontruncated reconstructors for the eight stars and two stars scenarios. The RMS WFE are mentioned in the legend. The value in brackets is the RMS WFE excluding the tip and tilt modes.

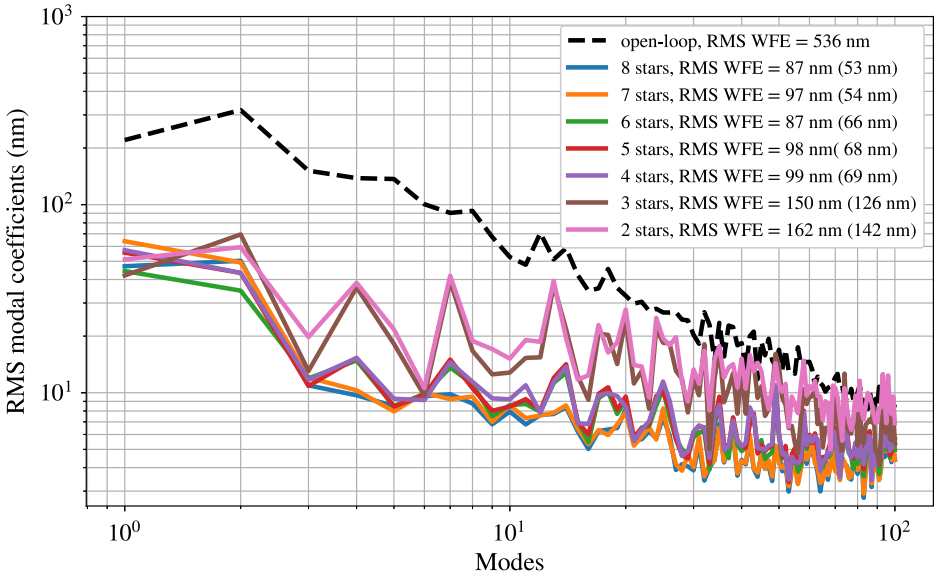

Fig. 11 The RMS value of the modal coefficients versus the modes for varying number of stars. The RMS WFE are mentioned in the legend. The value in brackets is the RMS WFE excluding the tip and tilt modes.

However, clustering and jump of the performance may be noted from the plot. This is because the modal basis is defined over the entire metapupil, as mentioned earlier. Some specific modes may not be adequately seen by the WFS, depending on the non-illuminated regions of the metapupil. Controlling these modes is possible with lower gain values. For this experiment, we have not individually tuned the gain values for individual modes. The gain values are split into three sets, as mentioned earlier, optimizing to produce the best performance for each asterism scenario. Note, however, that within each set, the gain value has the same scalar value. We are able to set relatively higher gain values and have the loop stable when the $\mathbb{M}$ is closer to full, even for the higher order modes. In contrast, for the two and three stars asterisms, with correspondingly fewer illuminated subapertures, we could only set relatively low gain values for the higher order modes (modes > 50).

In contrast to Fig. 10, note that all 100 modes were corrected for the two stars asterism as well. This is due to the fact that we carefully optimized the gain vector, thereby allowing a stable loop. In addition, in this case, the two stars were illuminating different regions of the metapupil and illuminating more number of subapertures. Although the correction is relatively poor for the two stars asterism, the fact that there is decent correction, which confirms that the partial illumination algorithm works.

4.2 *On-Sky Tests*

The final assessment of the performances of any AO system should come from on-sky testing. We have tested our implementation of the partial illumination solution in this way during LN commissioning. The goals were to verify the software compatibility of our solution with the rest of the LN MCAO system, to test the creation of the partial illumination mask, to verify the extraction of the daughter-$\mathbb{IM}$ and the uploading of the truncated reconstructor for the current K-mirror angle, and to check the HWS closed-loop performance with partial illumination.

During the second (June 2017) and third (January 2018) LN commissioning runs, we demonstrated the basic operation and functionality of the partial illumination code. This included the software compatibility of our solution with the high-layer wavefront sensing service and LN MCAO software architecture, in general, creation of the partial illumination, and the extraction of the daughter-$\mathbb{IM}$.

During the fourth commissioning run (April 2018), we successfully tested the CCD tracking algorithm that maintains the optical conjugation while observing. Also, both ground- and high-layer loops were stably closed, providing considerable improvement of the science image. One of the science targets was NGC 2281. A total of nine stars were acquired to measure the atmospheric turbulence. Figure 12 shows the asterism of stars and the processed NIR images of the central star. The ground-layer was closed using 50 modes. The ground-layer adaptive optics (GLAO) image measured a SR of $\sim$7.7% (K-band). 497 out of 616 subapertures within the metapupil were illuminated using five stars acquired by the HWS. Note that the central star, NGC 2281, was also one of the high-layer reference stars. We were able to close the high-layer loop stably with 40 modes, starting from a stable, ground-layer corrected wavefront. We measured the SR of the MCAO image to be $\sim$22% (K-band). The peak of the PSF (in K-band) jumped by a factor of $\sim$2.8 from GLAO to MCAO.

For estimating the on-sky, partial illumination performance, we downloaded a set of dmCommands each time that we closed the high-layer loop with different number of modes, each time optimizing the gain vector. Note that these data were taken very closely spaced in time, and we assume the atmosphere remained more or less the same then. From the dmCommands, we estimated the modal coefficients. Figure 13 shows the RMS value of the modal coefficients as a function of the modes for the same target. We overplotted each sets of data to check if there is any performance degradation while closing higher number of modes. As we close higher number of modes, starting from 10 to 50, the low-order modes are always corrected by the similar amount. There is no degradation in performance in the low-order modes while the high-spatial frequency modes are also corrected.

We remind that the acquisition of the NIR data (Fig. 12) and the WFS data used to make the plot in Fig. 13 were taken simultaneously or in very closely spaced time. While acquiring the

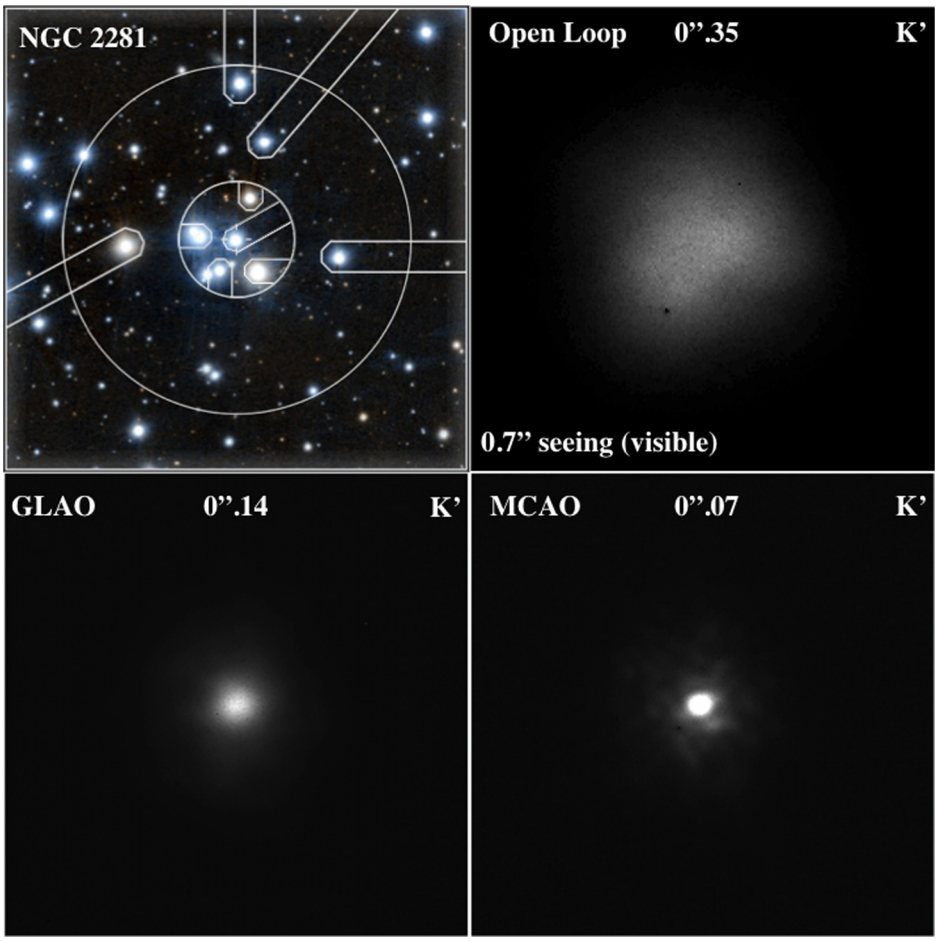

Fig. 12 Guide star acquisition field (upper left) and near infrared science images showing the on-sky verification of the partial illumination solution. Four and five stars were acquired using with the GWS (outer circle) and HWS (inner circle), respectively. While 50 modes were closed by the GWS, 40 modes were closed by the HWS. The open-loop seeing of 0".35 in the K' band (visible seeing of 0".7) was reduced to 0".14 with the ground-layer closed and to 0".07 with both loops closed (all values full width at half-maximum). Note that the open-loop image is stretched by a factor of 10 for greater visibility. The FoV of the NIR images is 2×2 square arcsecond. The top-left image of NGC 2281 is adapted from PanSTARRS-DR1.

high-layer data, the science image was continuously monitored and improvement of the PSF and its increasing peak value were visually confirmed. The RMS WFE corrected by the HWS is noted in Fig. 13. For comparison, we have also overplotted the dynamic open-loop RMS WFE of 536 nm applied in the lab (see Sec. 4 for details). Evidently, the on-sky power spectrum is similar to that of the artificial Kolmogorov one that we used for our lab studies. The high-altitude DM was introducing a WFE of 768 nm, which mostly corrected the incoming turbulence. The on-sky WFS data and the improvement in the NIR image demonstrate that our solution to the partial illumination is producing a good and stable correction.

In the June 2018 commissioning run, we continued to test and optimize the high-layer loop with fainter reference stars. Also, we increased the HWS CCD binning. For example, we selected a target that had only two off-axis reference stars. With 2×2 binning, we were able to close 20 modes stably.

We have demonstrated the real-time extraction of the daughter-$\mathbb{IM}$s, as well as the calculation and upload of the reconstructors needed for each $\theta°$ of sky rotation. We also verified that the partial illumination solution is binning generic, that is, the algorithm behaves properly for all CCD binning settings. Although the quantitative analysis of some data is still pending, we were able to establish that the solution for the partial illumination issue works well for the usual Kolmogorov spectrum of atmosphere, and the correction is good enough to see a considerable improvement in the science image. In the upcoming LN commissioning runs, we will be testing targets with fainter reference stars and one star only asterisms.

5 Conclusions and Future Prospects

Our solution to the partial illumination issue is simple, practical, and effective. Depending on the brightness and the spatial distribution of the stars, the quality of correction varies. Nevertheless, we are able to close and produce a stable loop by controlling the gain vector both in lab and on-sky.

We demonstrated that more illuminated subapertures lead to better correction and lower WFE. Also, in those scenarios, more modes can be controlled with higher gain values. Experience suggests that it is better to have more-or-less equal brightness stars (providing more-or-less uniform SNR across the metapupil). Obviously, the brighter the stars, the better.

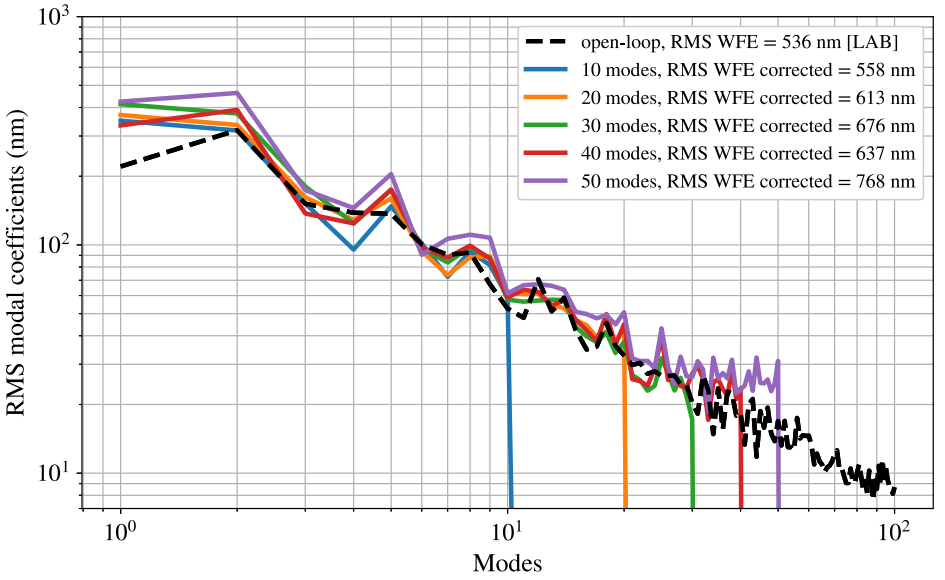

Fig. 13 The RMS value of the modal coefficients versus the modes for the asterism shown in Fig. 12. Although we closed up to 50 modes in the high layer, we noticed instabilities arising for modes higher than 40. Therefore, for the IR image shown in the bottom-right corner of Fig. 12, only the first 40 modes were closed. The RMS WFE are mentioned in the legend.

In April 2017, LN started MCAO operations on-sky with partial illumination. We will continue on-sky testing and optimization in the upcoming commissioning runs.

So far, we have used only a single SNR threshold to define the illuminated subapertures across the entire metapupil. Actually, instead of using a single threshold, we can weight the subapertures according to the relative intensity using minimum mean square error (MMSE) regularization.[50] The MMSE formulation, already developed for MCAO applications,[51] takes into account both the C_n^2 vertical profile and WFS noise. In our case, since the ground- and high-layer loops are independent, we just need the SNR map to properly weight the slope vector. Eventually, implementing the MMSE formulation could improve the robustness and quality of the MCAO correction.

Layer-oriented MCAO has the advantage of receiving direct AO telemetry for the individual conjugated layers from the respective WFSs. This can be potentially used to estimate the wind speed and direction for the layers. Not only is this information valuable in profiling the atmosphere above the telescope pupil but it can also be used to effectively reduce the time-lag between the wavefront sensing and the correction. In other words, we may be able to predict the future wavefront, knowing the current wavefront and the wind vector. In the case of the HWS, this prediction can be even more powerful. Nonilluminated subapertures, those for which we have no wavefront information, may be virtually filled using the "wind-predictive wavefront control."[34] Figure 14 illustrates this schematically.

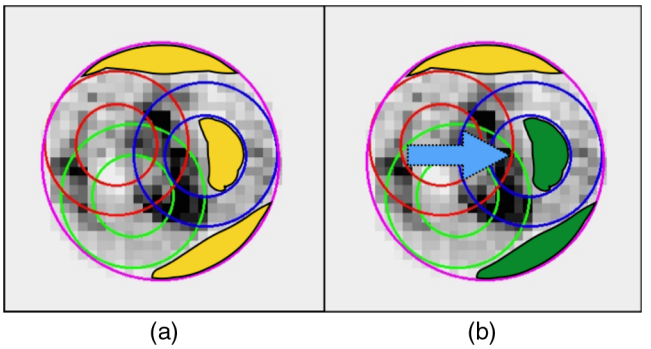

Fig. 14 Virtually filling subapertures using wind-predictive wavefront control on the high layer loop. (a) The partially illuminated metapupil. The yellow shaded regions represent the nonilluminated subapertures. (b) A favorable wind direction (blue arrow) allows us to virtually fill in some of the nonilluminated subapertures, represented by the green shaded regions.

We plan to implement wind-predictive wavefront control for the LN MCAO system in multiple phases. As a first step, we will try our algorithms with the ground-layer sensors, where all the subapertures are always illuminated. Implementing it on the HWS loop service could be trickier, as we would have to first estimate the total number of illuminated subapertures, including those that can be filled virtually, and then, weigh them depending on their SNR. Only thereafter can we generate and register the appropriate reconstructor. However, we believe that wind-predictive wavefront control could improve both the performance and stability of the HWS loop.

Acknowledgments

KKRS thanks Jürgen Berwein for integrating the partial illumination code to the LN software package. KKRS also thanks Benoit Neichel, Peter Bizenberger, and Micah Klettke for fruitful discussions and support. The authors express their sincere gratitude to the LBT mountain crew for their continuing support and dedication, which made our remote and onsite activities very smooth and effective. The authors thank the anonymous referees for their useful comments and suggestions.

The LBT is an international collaboration among institutions in the United States, Italy, and Germany. The LBT Corporation partners are the University of Arizona on behalf of the Arizona university system; Istituto Nazionale di Astrofisica, Italy;

LBT Beteiligungsgesellschaft, Germany, representing the Max Planck Society, the Astrophysical Institute Potsdam, and Heidelberg University; The Ohio State University; The Research Corporation, on behalf of the University of Notre Dame, University of Minnesota, and University of Virginia.

This work has made use of data from the European Space Agency (ESA) mission Gaia,[52] processed by the Gaia Data Processing and Analysis Consortium (DPAC).[53] Funding for the DPAC has been provided by national institutions, in particular, the institutions participating in the Gaia Multilateral Agreement.

This research made use of Astropy, a community-developed core Python package for Astronomy, and the IPython package. Furthermore, the author used the following python packages extensively within the partial illumination code: NumPy, Matplotlib, and SciPy. This research has made use of NASA's Astrophysics Data System Bibliographic Services.

References

1. J. M. Beckers, "Increasing the size of the isoplanatic patch with multiconjugate adaptive optics," in *Eur. South. Obs. Conf. and Workshop Proc.*, M.-H. Ulrich, Ed., Vol. **30**, p. 693 (1988).
2. J. M. Beckers, "Detailed compensation of atmospheric seeing using multiconjugate adaptive optics," *Proc. SPIE* **1114**, 215–217 (1989).
3. R. Ragazzoni, E. Marchetti, and F. Rigaut, "Modal tomography for adaptive optics," *Astron. Astrophys.* **342**, L53–L56 (1999).
4. R. Ragazzoni, E. Marchetti, and G. Valente, "Adaptive-optics corrections available for the whole sky," *Nature* **403**, 54–56 (2000).
5. E. Marchetti et al., "MAD the ESO multi-conjugate adaptive optics demonstrator," *Proc. SPIE* **4839**, 317–328 (2003).
6. E. Marchetti et al., "MAD: practical implementation of MCAO concepts," *C. R. Phys.* **6**, 1118–1128 (2005).
7. E. Marchetti, "MAD upgrade proposal: concept & correction performance," in *MAD and Beyond Workshop*, ESO, Garching (2009).
8. S. Esposito et al., "AOF upgrade for VLT UT4: an 8 m class HST from ground," *Proc. SPIE* **9909**, 99093U (2016).
9. E. Diolaiti et al., "MAORY: adaptive optics module for the E-ELT," *Proc. SPIE* **9909**, 99092D (2016).
10. G. Herriot et al., "NFIRAOS: first facility AO system for the Thirty Meter Telescope," *Proc. SPIE* **9148**, 914810 (2014).
11. F. Rigaut and B. Neichel, "Multiconjugate adaptive optics for astronomy," *Annu. Rev. Astron. Astrophys.* **56**(1), 277–314 (2018).
12. F. Rigaut et al., "Gemini multiconjugate adaptive optics system review - I. Design, trade-offs and integration," *Mon. Not. R. Astron. Soc.* **437**, 2361–2375 (2014).
13. B. Neichel et al., "Gemini multiconjugate adaptive optics system review - II. Commissioning, operation and overall performance," *Mon. Not. R. Astron. Soc.* **440**, 1002–1019 (2014).
14. T. M. Herbst et al., "The LINC NIRVANA multi-conjugate adaptive optics imager," *in preparation* (2019).
15. T. M. Herbst et al., "LINC-NIRVANA: a Fizeau beam combiner for the large binocular telescope," *Proc. SPIE* **4838**, 456–465 (2003).
16. T. M. Herbst et al., "Novel adaptive optics on the pathway to ELTs: MCAO with LINC-NIRVANA on LBT," in *2nd Int. Conf. Adapt. Opt. for Extrem. Large Telesc.*, p. 20, (2011).
17. T. M. Herbst et al., "Installation and commissioning of the LINC-NIRVANA near-infrared MCAO imager on LBT," *Proc. SPIE* **10702**, 107020U (2018).
18. M. Tallon, R. Foy, and J. Vermin, "3-D wavefront sensing for multiconjugate adaptive optics," in *Eur. South. Obs. Conf. and Workshop Proc.*, Vol. **42**, p. 517 (1992).
19. R. Ragazzoni, J. Farinato, and E. Marchetti, "Adaptive optics for 100-m-class telescopes: new challenges require new solutions," *Proc. SPIE* **4007**, 1076–1087 (2000).
20. C. Arcidiacono et al., "Toward the first light of the layer oriented wavefront sensor for MAD," *Mem. Soc. Astron. Ital.* **78**, 708 (2007).
21. T. M. Herbst et al., "Commissioning multi-conjugate adaptive optics with LINC-NIRVANA on LBT," *Proc. SPIE* **10703**, 107030B (2018).
22. R. Ragazzoni, "Pupil plane wavefront sensing with an oscillating prism," *J. Mod. Opt.* **43**, 289–293 (1996).
23. R. Ragazzoni et al., "Multiple field of view layer-oriented adaptive optics. Nearly whole sky coverage on 8 m class telescopes and beyond," *Astron. Astrophys.* **396**, 731–744 (2002).
24. J. Farinato et al., "The multiple field of view layer oriented wavefront sensing system of LINC-NIRVANA: two arcminutes of corrected field using solely natural guide stars," *Proc. SPIE* **7015**, 70155J (2008).
25. C. Arcidiacono et al., "Sky coverage for layer-oriented MCAO: a detailed analytical and numerical study," *Proc. SPIE* **5490**, 563–573 (2004).
26. A. Tokovinin and E. Viard, "Limiting precision of tomographic phase estimation," *J. Opt. Soc. Am. A* **18**, 873–882 (2001).
27. R. Ragazzoni et al., "Multiple field of view layer oriented," in *Eur. South. Obs. Conf. and Workshop Proc.*, Vol. **58**, p. 75 (2002).
28. A. Wirth et al., "Deformable mirror technologies at AOA Xinetics," *Proc. SPIE* **8780**, 87800M (2013).
29. R. Ragazzoni and J. Farinato, "Sensitivity of a pyramidic wave front sensor in closed loop adaptive optics," *Astron. Astrophys.* **350**, L23–L26 (1999).
30. V. Viotto et al., "Expected gain in the pyramid wavefront sensor with limited Strehl ratio," *Astron. Astrophys.* **593**, A100 (2016).
31. C. Vérinaud et al., "Layer oriented multi-conjugate adaptive optics systems: performance analysis by numerical simulations," *Proc. SPIE* **4839**, 524–535 (2003).
32. T. Bertram et al., "Wavefront sensing in a partially illuminated, rotating pupil," *Proc. SPIE* **9148**, 91485M (2014).
33. K. K. R. Santhakumari et al., "Solving the MCAO partial illumination issue and laboratory results," *Proc. SPIE* **9909**, 99096M (2016).
34. K. K. R. Santhakumari et al., "On-sky verification of a solution to the MCAO partial illumination issue and wind-predictive wavefront control," *Proc. SPIE* **10703**, 107035L (2018).
35. F. Arenou et al., "Gaia data release 2. Catalogue validation," *Astron. Astrophys.* **616**, A17 (2018).
36. A. G. A. Brown et al., "Gaia data release 2. Summary of the contents and survey properties," *Astron. Astrophys.* **616**, A1 (2018).
37. T. Prusti et al., "The Gaia mission," *Astron. Astrophys.* **595**, A1 (2016).
38. M. Riello et al., "Gaia Data Release 2. Processing of the photometric data," *Astron. Astrophys.* **616**, 16–24 (2018).
39. D. S. Durie, "A compact derotator design," *Opt. Eng.* **13**, 119 (1974).
40. A. Brunelli et al., "Tips and tricks for aligning an image derotator," *Proc. SPIE* **8446**, 84464L (2012).
41. J. Moreno-Ventas et al., "Optical integration and verification of LINC-NIRVANA," *Proc. SPIE* **9147**, 91473V (2014).
42. T. M. Herbst et al., "MCAO with LINC-NIRVANA at LBT: preparing for first light," *Proc. SPIE* **9909**, 99092U (2016).
43. C. Arcidiacono et al., "Numerical control matrix rotation for the LINC-NIRVANA multiconjugate adaptive optics system," *Proc. SPIE* **7736**, 77364J (2010).
44. C. Arcidiacono et al., "The calibration procedure of the LINC-NIRVANA ground and high layer WFS," *Proc. SPIE* **10703**, 107034R (2018).
45. J. W. Hardy, "Adaptive Optics for Astronomical Telescopes," *Phys. Today* **53**(4), 69 (1998).
46. M. Klettke et al., "CCD tracking for gravity flexure compensation on LINC NIRVANA," in preparation (2019).
47. J.-P. Véran, "Control of the unilluminated deformable mirror actuators in an altitude-conjugated adaptive optics system," *J. Opt. Soc. Am. A* **17**, 1325–1332 (2000).
48. E. H. Moore, "On the reciprocal of the general algebraic matrix," *Bull. Am. Math. Soc.* **26**, 394–395 (1920).
49. R. Penrose, "A generalized inverse for matrices," *Math. Proc. Cambridge Philos. Soc.* **51**(3), 406–413 (1955).
50. B. L. Ellerbroek, "First-order performance evaluation of adaptive-optics systems for atmospheric-turbulence compensation in extended-field-of-view astronomical telescopes," *J. Opt. Soc. Am. A* **11**, 783–805 (1994).
51. T. Fusco et al., "Optimal wave-front reconstruction strategies for multiconjugate adaptive optics," *J. Opt. Soc. Am. A* **18**, 2527–2538 (2001).
52. European Space Agency, https://www.cosmos.esa.int/gaia (2019).
53. European Space Agency, https://www.cosmos.esa.int/web/gaia/dpac/consortium (2019).

Kalyan Kumar Radhakrishnan Santhakumari is a postdoctoral fellow at the INAF-Astronomical Observatory of Padova, Italy. In 2017, he obtained a PhD degree in astronomy and astrophysics from Ruprecht-Karls-Universität Heidelberg, Germany, working on the adaptive optics system of the LINC-NIRVANA instrument at the Max Planck Institute for Astronomy, Heidelberg. He has experience working on the AO calibration strategies, commissioning AO systems, and presently, contributing to the various adaptive optics projects (LINC-NIRVANA, INGOT, MAVIS, and SHARK-NIR).

Carmelo Arcidiacono received the PhD in astronomy in 2005, became a staff researcher at the INAF on 2011, and is currently working at the INAF-Astronomical Observatory of Padova. Since 2001, he has been contributing to the development of astronomical instrumentation. His primary expertise is concerning adaptive optics, focusing on numerical simulations, laboratory testing, instrument commissioning, data analysis, and science targets definition. He is the instrument scientist of MAORY (ELT) and leads the Science Operation Working Group.

Thomas Bertram received his PhD in physics from the University of Cologne, Germany, in 2007. In 2008, he joined the Max Planck Institute for Astronomy in Heidelberg, Germany, where he develops instrumentation and adaptive optics systems for professional ground-based astronomical observatories. He is the system engineer for LINC-NIRVANA, and since 2016, the single conjugate adaptive optics system lead for METIS, the mid-infrared instrument for the Extremely Large Telescope.

Florian Briegel received his master of computer science from Karlsruhe Institute of Technology (former Technische Universität Karlsruhe) in 1992. In 1998, he joined the Max Planck Institute for Astronomy (MPIA) in Heidelberg, Germany, where he develops instrumentation control and adaptive optics software for professional ground-based astronomical observatories. Since 2009, he is the head of the software development department at MPIA.

Thomas M. Herbst is a senior staff astronomer and research group leader at the Max Planck Institute for Astronomy in Heidelberg. He received his PhD from Cornell University and completed a postdoctoral at the University of Hawaii before moving to the MPIA. His science interests are in the field of high angular resolution astronomy, with an emphasis on star formation. He is the principal investigator of the LINC-NIRVANA instrument.

Roberto Ragazzoni received a degree in astronomy at the University of Padova in 1990. He worked at the Astronomical Observatory of Padova (Italy), the Steward Observatory in Tucson (Arizona), the Center for Astrophysics of the UCSD (California), the Max Planck Institute for Astronomy in Heidelberg (Germany), and at the Astrophysical Observatory of Arcetri in Florence (Italy). He was awarded of the Wolfgang Paul Prize from the Alexander von Humboldt Society in 2001. His main area of scientific interest is conceiving, building, and operating astronomical instrumentation for the ground or the outer space. Currently, he is the director of the Astronomical Observatory of Padova.